Supplementary Information for

Tailoring the Wadsley-Roth Crystallographic Shear Structures for High-Power Lithium-ion Batteries

Panpan Jing[a,b,†], Mengting Liu[b,c,†], Hsin-Pei Ho[d], Yifan Ma[e], Weibo Hua[c], Haohui Li[a], Nan Guo[a], Yong Ding[b], Weilin Zhang[b], Hailong Chen[e], Bote Zhao[b,f,*], Jenghan Wang[d,*], Meilin Liu[b,*]

[a]*School of Materials Science and Engineering, Shaanxi Key Laboratory of Green Preparation and Functionalization for Inorganic Materials, Shaanxi University of Science & Technology, Xi'an, Shaanxi Province, 710021, China*

[b]*School of Materials Science and Engineering, Georgia Institute of Technology, Atlanta, GA, 30332, USA*

[c]*School of Chemical Engineering and Technology, Center of Nanomaterials for Renewable Energy, State Key Laboratory of Electrical Insulation and Power Equipment, School of Electrical Engineering, Xi'an Jiaotong University, Xi'an, Shaanxi 710049, China*

[d]*Department of Chemistry, National Taiwan Normal University, Taipei 116, Taiwan*

[e]*The Woodruff School of Mechanical Engineering, Georgia Institute of Technology, Atlanta, GA, 30332, USA*

[f]*School of Environment and Energy, South China University of Technology, Guangzhou 510006, China*

†These authors contributed equally: Panpan Jing, Mengting Liu

*botezhao@scut.edu.cn, jenghan@ntnu.edu.tw, meilin.liu@mse.gatech.edu

1. Experimental details

1.1 Starting chemical reagents

In this work, the niobium pentoxide (Nb_2O_5, Sigma-Aldrich, 99.9%), tungsten trioxide nanoparticles (WO_3, Sigma-Aldrich, ≥99%), anatase titanium dioxide (a-TiO_2, Sigma-Aldrich, 99.7%), pyrrole liquid (C_4H_5N, Sigma-Aldrich, 98%), graphene powders (2DM company), sodium dodecyl sulfate ($NaSO_4C_{12}H_{25}$, Sigma-Aldrich, 98.5%) and ammonium persulfate ($(NH_4)_2S_2O_8$, Sigma-Aldrich, ≥98%) were used as raw materials without further purification.

1.2 Sample preparation

(1) TNWO bulk. The TNWO bulk powders were synthesized via a traditional solid-state sintering from starting materials of Nb_2O_5, WO_3 and a-TiO_2, of which the mole ratio was set as 13:4:1, followed by hand-grinding. In details, the starting materials with a small amount of DI water and ethanol were blended thoroughly for 10 hours by a roller mixer (FRITSCH PULVERISETTE 7 premium line). After complete drying, the well-premixed powders were pressed into pellets with a diameter of 13 mm followed by sintering at 1100 ^oC for 5 h in a box furnace under air atmosphere. The rising rates were set to 5 $^oC\ min^{-1}$. After hand-grinding the cooled pellets by using a mortar and pestle, TNWO bulk powders was obtained.

(2) TNWO@G-C composite. The as-prepared TNWO powders were ball milled with 2 wt% of graphene powders at 500 rpm for 2.5 h by the ball miller. Then 160 mg of the collected mixture and 8 mg of $NaSO_4C_{12}H_{25}$ were dissolved in a 20 ml of DI water followed by ultrasonic treating for 1.5 h. Subsequently, 20 µl of pyrrole liquid was injected into the suspension. Stirring for 0.5 h later, 4 ml of $(NH_4)_2S_2O_8$ aqueous solution in 0.1 M was added further and stirred for another 1 h. The treated powders were collected by centrifuging followed by drying in Air for overnight and heating in Ar at 800 ^oC in a tube furnace for 2 hours. As a result, the TNWO@G-C composite was obtained.

1.3 Basic characterizations

The phase components of as-prepared samples were determined by using a high-energy synchrotron radiation source (λ= 0.1948 Å) at beamline 28ID-2 at the National Synchrotron Light Source II (NSLS-II) at the Brookhaven National Laboratory (BNL, Upton, NY, USA), a powder X-ray diffraction (XRD, X'Pert PRO Alpha-1) with Cu Kα radiation, an aberration-corrected scanning transmission electron microscopy (STEM, Hitachi HD 2700), a high-resolution transmission electron microscopy (HRTEM, FEI G2 Tecnai F30) and selective area electron diffraction (SAED), a Raman spectroscopy (Renishaw RM1000) with a 514 nm laser excitation. Rietveld refinement was performed against the synchrotron XRD data by using EXPGUI suite of GSAS code[1] and the crystal structure was visualized by using VESTA software. A field-scattering scanning electron microscopy

(FESEM, a Hitachi SU8010) was applied to observe the morphological features. The surface chemical elemental compositions and chemical states were analyzed by using an X-ray photoelectron spectroscopy (XPS, Physical Electronics PHI 5802) with Mg Kα radiation. Especially, a Q600 SDT system (from TA Instruments) was used for thermal gravimetric analysis (TGA) testing to evaluate the total mass of graphene and carbon content in the TNWO@G-C composite.

1.4 Electrochemical performance evolutions

1.4.1 Anode fabrication and half-cell assembling

In order to evaluate the Li^+ storage performance of the as-prepared TNWO bulk powders, TNWO@G-C composite and control samples, all of them were separately used as active materials of working electrodes and assembled into the CR2032 coin type half-cells in an argon-filled glovebox. To prepare the working electrodes, typically, the active materials, extra conducting agent of super P and binder of polyvinylidene fluoride in a weight ratio of 80:10:10 with a balanced amount of N-methyl-2-pyrrolidone (Sigma-Aldrich, 99.5%, anhydrous) were uniformly blended under a continuous stirring at room temperature in a vial with a volume of 10 ml to get an uniform slurry at first. Secondly, the slurry was scraped on a Cu foil and dried at 90 ^oC in a vacuum oven for overnight. Finally, the anodes were obtained by cutting the foil into discs with a diameter of 1 cm. The average mass loadings of the active materials were controlled at two values of about 1.5 and 2.5 mg cm^{-2}, respectively. Taking the TNWO electrode as an example, subsequently, the half cells were assembled as a down-up sequence of aluminum coated can, working electrode (TNWO), separator (glass microfiber membrane, Whatman), adding liquid electrolyte (1 M of $LiPF_6$ in ethylene carbonate/dimethyl carbonate with 1:1 in volume ratio, Sigma-Aldrich), metallic Li foil counter and reference electrode, steel spacer with a thickness of 1 mm, steel spring and steel cap and gasket.

1.4.2 Electrochemical measurements

(1) Cyclic voltammetry (CV) and electrochemical impedance spectroscopy (EIS) test

A Solartron 1255 HF frequency response analyzer was used to record the CV curves and EIS spectra of the as-assembled cells. The frequency range for the EIS testing was set from 100 MHz to 0.01 Hz. For the CV testing, the voltage window and scan rate were set as 1 ~ 3 V and 0.01 mV s^{-1} (0.3, 0.5, 0.7, 0.9, 1.1, 1.5, 2.0 and 2.5 mV s^{-1}), respectively. The pseudocapactive behavior can be revealed by the relationship between redox peak current and scan rate of these CV curves, ie. $I_P = av^b$,[2] in where the value of the exponent *b* of 0.5 is usually representative of a diffusion-controlled behavior, while *b* value of 1.0 is representative of a capacitive-controlled behavior, of which the above power-law formula can be deformed into $logI_P = loga + blogv$.[3] To further

quantify the diffusive and capacitive capacities, the liner plots of $I(V)/v^{1/2}$ vs. $v^{1/2}$ at various potentials are acquired using the equation $I(V) = k_1 v + k_2 v^{1/2}$.

(2) Rate-capability and long cycling test

A NEWARE BTS-610 8-channel battery test system (Shenzhen, China) was applied to recording the galvanostatic discharge-charge (GCD) curves to investigate the rate-capability and long cycling performance. The voltage window and current density were set as 1 ~ 3 V and 0.05 A g^{-1}, respectively. The current densities during the rate-capability testing were successively set as 0.05, 0.1, 0.2, 0.5, 1, 2, 5, 10, 15 and 0.05 A g^{-1}. The long-term cycling tests were performed at the current densities of both 1 and 5 A g^{-1} after five-cycle activation at 0.05 A g^{-1}. Galvanostatic intermittent titration technique (GITT) curves were recorded at a current pulse width of 0.5 h, a rest step of 6 h and a current density of 50 mAh g^{-1}. The Li^+ diffusion coefficients was extracted from the GITT profile according to the equation of $D_{Li^+} = \frac{4}{\pi\tau}\left(\frac{m_B V_M}{M_B S}\right)^2\left(\frac{\Delta E_s}{\Delta E_\tau}\right)^2$ (D_{Li^+}, M_B, m_B, V_M, S, ΔE_s and ΔE_τ represents the Li^+ diffusion coefficient, molecular weight, mass, molar volume, surface area, steady potential difference in the plateau and the voltage drop between during the relaxation of the electrode, respectively).[4,5] During the calculation, because the different particle sizes, porous structure and solid-liquid interfaces of the electrode result in that it's hard to extract the physically absolute Li^+ diffusion coefficients, a diffusion length $L = \frac{m_B V_M}{M_B S}$ is defined as the bridge. Thus, a qualitative Li^+ diffusion coefficient was calculated from the equation of $\frac{D_{Li^+}}{L^2} = \frac{4}{\pi\tau}\left(\frac{\Delta E_s}{\Delta E_\tau}\right)^2$.[5]

(3) Operando high-energy synchrotron XRD test

The electrochemical cell in a transmission mode used for the operando synchrotron XRD test (at beam line 28ID-2) at the National Synchrotron Light Source II at the Brookhaven National Laboratory) consists of two-sided Be windows, which is similar to those used in any previous reports[6]. The mass of the TNWO bulk material on the electrode with 12 mm in diameter is about 3 mg. During the test, the cell was began with discharging from open circuit voltage and then charging in the voltage window of 1.0 ~ 3 V (vs. Li/Li^+) at a current density of 0.2 A/g. The corresponding XRD patterns were collected at a scan rate of ~2 min/scan. Rietveld refinement was performed against the XRD patterns using the FULLPROF program to obtain the changes of the crystallographic parameters and phase fraction.[7,8]

1.5 Computational section

Vienna Ab Initio Simulation Package (VASP)[9-11] and a density functional theory (DFT) based package with 3D periodic boundary condition were employed in the present calculations for structural optimization, energetic calculation and electronic structure analysis. The exchange-correlation functional was based on generalized gradient approximation (GGA) with Perdew-Wang 1991 pseudopotentials, so called GGA-PW91.[12,13] Core electrons were simulated by pseudo-potential implemented in VASP. Valance electrons were expanded by plane-wave basis with 600-eV cutoff energy in projector-augmented wave method (PAW).[14,15] Brilloiun-zone integrations were sampled in the reciprocal space with Monkhorst-Pack scheme at 0.05 × 2 (1/Å) interval.[16] The energetic and gradient convergences for structural optimization were set at 10-4 eV and 10^{-2} eV/Å, respectively. The supercells of NWO, TNWO and T-free TNWO were constructed by $Nb_{28}W_6O_{88}$, $Nb_{28}W_5Ti_1O_{88}$ and $Nb_{30}W_1Ti_1O_{80}$; all with two 4×4 corner-sharing [NbO_6] blocks. There were 24 pocket sites and 24 vertical window sites on each model for Li^+ accommodation; tetrahedral O sites in NWO and TNWO were not considered for the accommodation. A total for 48 Li^+ can be fully accommodated in those three models. There were 18 horizontal window sites for Li^+ transportation in those models.

2. Supplementary Figures

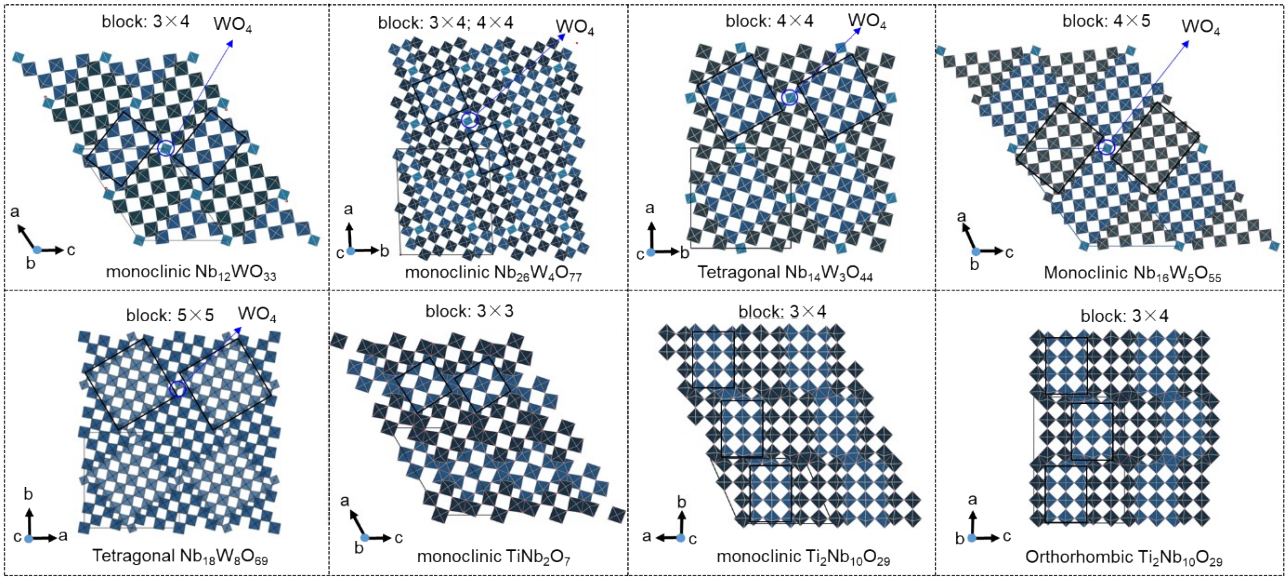

Figure S1. Schematic block structure models of typical Nb-W-O compounds ($Nb_{12}WO_{33}$, $Nb_{26}W_4O_{77}$, $Nb_{14}W_3O_{44}$, $Nb_{16}W_5O_{55}$ and $Nb_{18}W_8O_{69}$)[5,17-19] and Ti-Nb-O compounds ($TiNb_2O_7$ and $Ti_2Nb_{10}O_{29}$)[3,20]. Differently, every four nearest blocks of the Nb-W-O compounds are linked by a [WO_4] tetrahedron through corner-sharing, while the tetrahedron characteristic is not discovered in Ti-Nb-O compounds. In comparison, the Nb-W-O compounds generally have larger block dimensions with more [MO_6] octahedron than the Ti-Nb-O compounds. Moreover, the block size is increased with decreasing the atomic ratio of Nb to W.

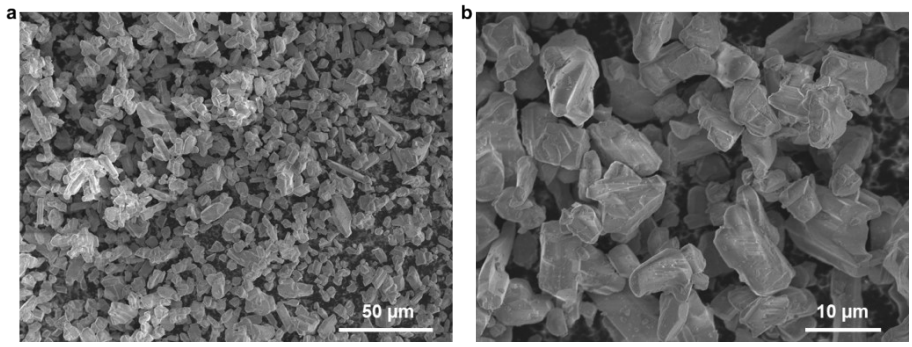

Figure S2. SEM images of the as-prepared TNWO bulk powders. Obviously, the powders are irregular particles with distinguished shape anisotropy and 5 ~ 10 μm in size.

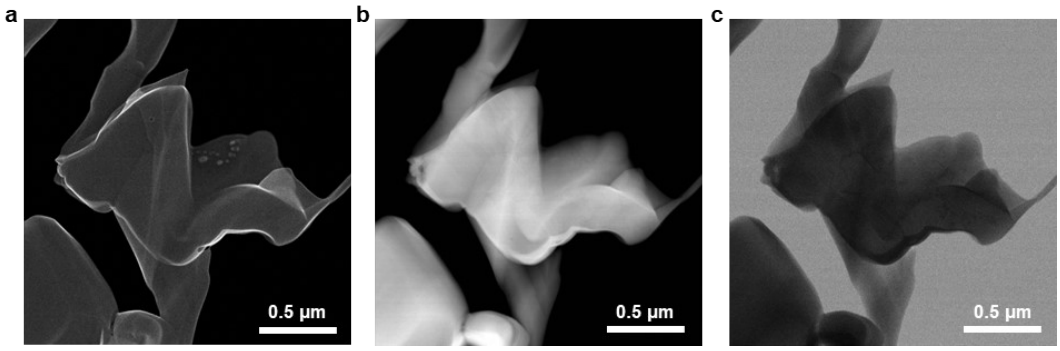

Figure S3. (a) SEM, (b) annular dark field TEM and (c) annular bright field TEM images of a TNWO grain for local atomic arrangement observation. The test specimens were prepared using focused ion beam (FIB) lift-out technique.

Table S1. Block structure comparison among the crystallographic shear niobium-based oxides.

Materials	Block type	Number of metal atoms per block	Number of vertical channel per block	Reference
Ti-Nb-W-O	3×4	12	6	This work
	4×4	16	9	
	3×6	18	10	
	4×5	20	12	
	3×7	21	12	
	4×6	24	15	
	3×8	24	14	
	5×5	25	16	
	3×9	**27**	**16**	
H-Nb_2O_5	3×4	12	6	21
	3×5	15	8	
$TiNb_2O_7$	3×3	9	4	20
$Nb_{12}O_{29}$	4×3	12	6	22
$MNb_{11}O_{29}$ (M = Fe、Al、Cr)	4×3	12	6	23,24
$Ti_2Nb_{10}O_{29}$	4×3	12	6	3
$Ti_2Nb_{14}O_{39}$	4×3	12	6	25
$TiNb_{24}O_{62}$	3×4	12	6	26
$Nb_{12}WO_{33}$	3×4	12	6	27
$Nb_{14}W_3O_{44}$	4×4	16	9	28
$Nb_{16}W_5O_{55}$	4×5	20	12	5
$Nb_{18}W_8O_{69}$	5×5	25	16	19
$V_3Nb_{17}O_{50}$	3×3	9	4	29

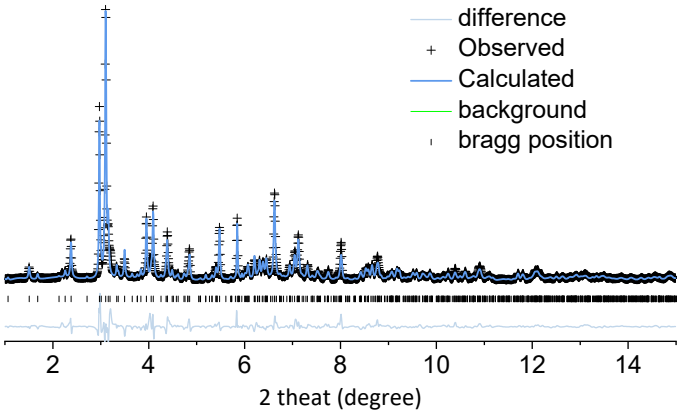

Figure S4. Synchrotron XRD pattern of the new TNWO bulk powders and refinement using space group *I*. According to the great agreement between the experimental data and the refinement data with only one set of diffraction peaks, clearly, the TNWO bulk sample is a single phase.

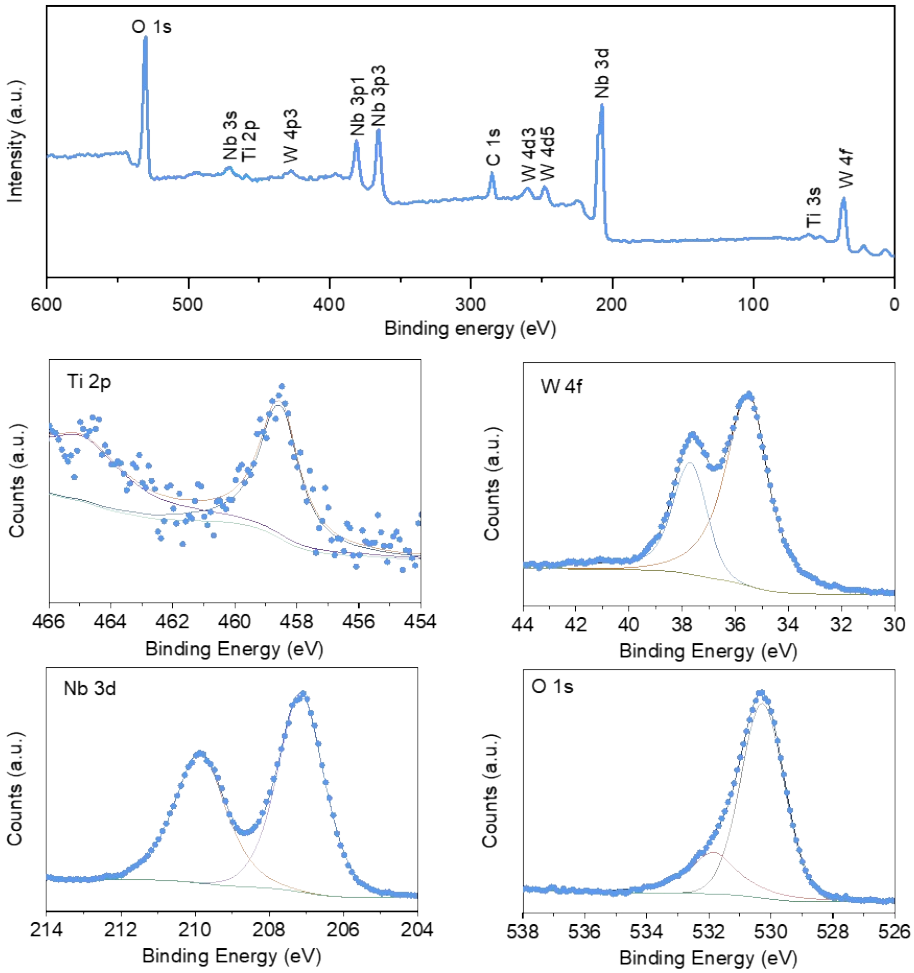

Figure S5. Full-scan XPS spectrum of the TNWO bulk powders and the high-resolution XPS spectra of Ti 2p, Nb 3d, W 4f, O 1s. Clearly, although the all metallic Ti, W and Nb elements are detected, the intensity of Ti is much lower than that of W and Nb. According to their peak positions and spin-orbit doublets, the Ti is dominated as Ti^{4+}, Nb is dominated as Nb^{5+} and W is dominated as W^{6+}.

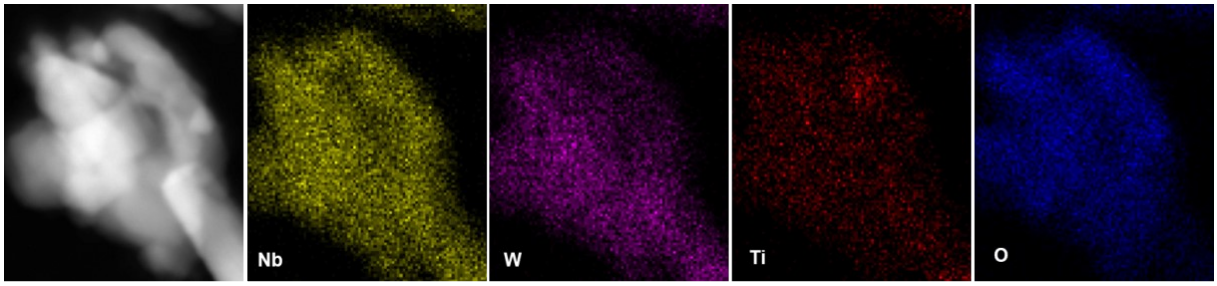

Figure S6. EDS elemental mappings of the TNWO bulk powders. Clearly, the Nb, W, Ti and O elements are uniformly distributed in the whole materials. One can notice that the amount of metal elements is followed the order of Nb>W>Ti.

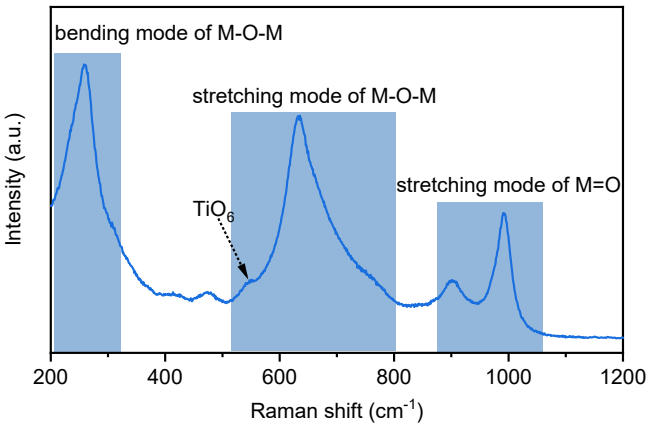

Figure S7. Raman spectrum of the as-prepared TNWO bulk powders. The peak centered at 260 cm^{-1} corresponds to the bending mode of M-O-M bonds (M represents Nb, W and Ti), while the peaks centered at 633.8 and 1000 cm^{-1} are singed to stretching mode of M-O-M bonds and M=O bonds, respectively.[21] Clearly, there is a weak shoulder peak at ~ 547.2 cm^{-1} can be assigned to the TiO_6 octahedron.

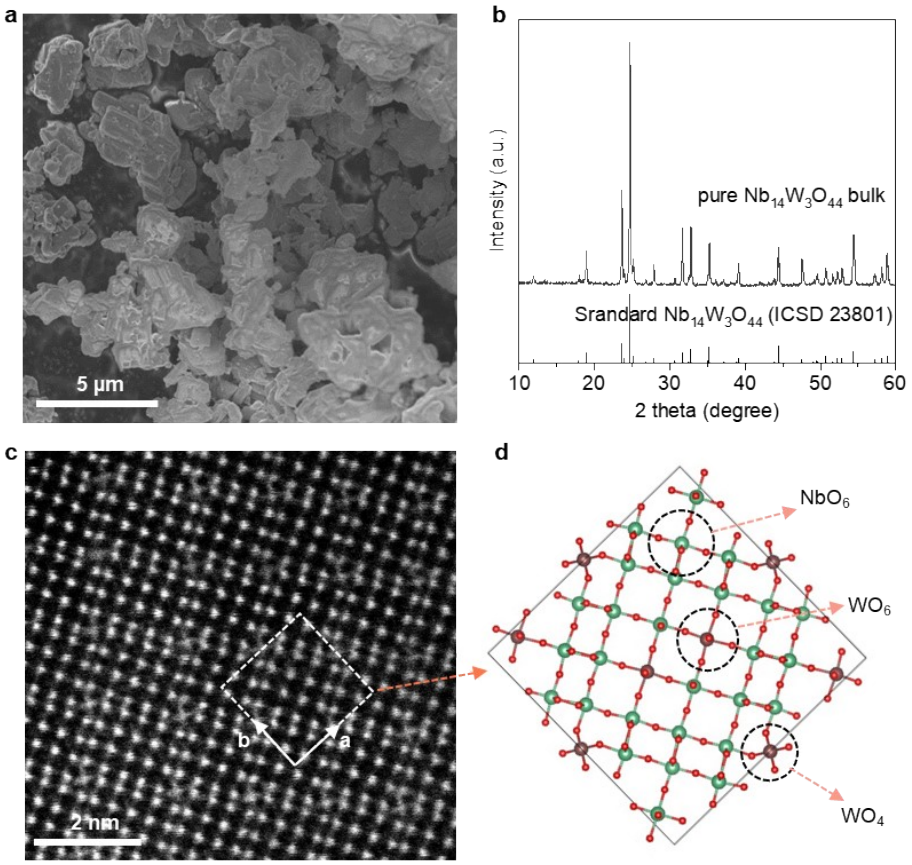

Figure S8. (a) SEM image, (b) powder XRD pattern, (c) HADDF-STEM image and (d) block scheme of as-prepared pure $Nb_{14}W_3O_{44}$ bulk material.

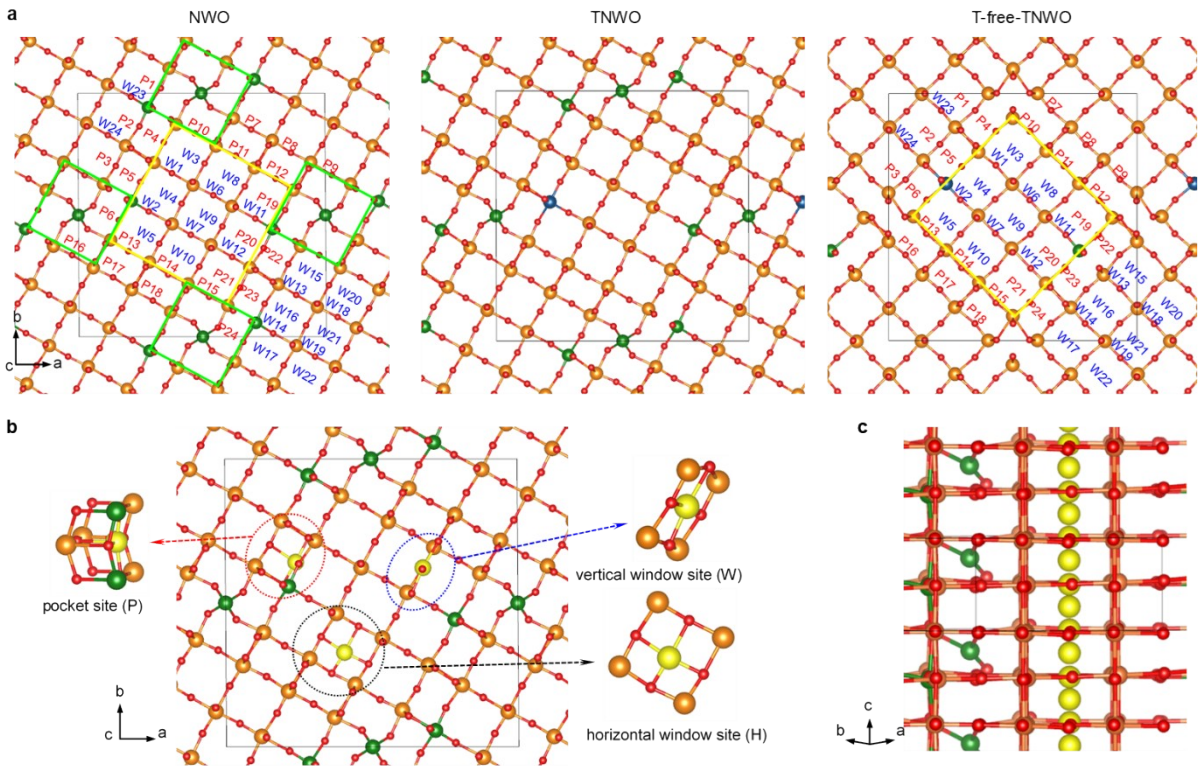

Figure S9. (a) Crystal structure models of NWO, TNWO and T-free-TNWO for computations. The 4×4 blocks are marked by yellow squares and WO_4 tetrahedra are marked by green squares. (b) Schemetic illustrations of the three kinds of Li^+ adsorptions sites, pocket (P), vertical window (W) and horizontal window (H) sites on NWO. Nb^{5+}, W^{6+}, Ti^{4+}, O^{2-} and Li^+ are represented in orange, green, navy blue, red and yellow balls. In the pocket sites, Li^+ can be bonded with five O^{2-} and located in the edge-sharing of blocks. Window sites, also known as square-planar sites, include both vertical and horizontal cavities, in which Li^+ will be bonded with four O^{2-} vertically and horizontally in the *ab* plane, respectively. (c) Schematic illustration of Li^+ adsorption along the c-axis.

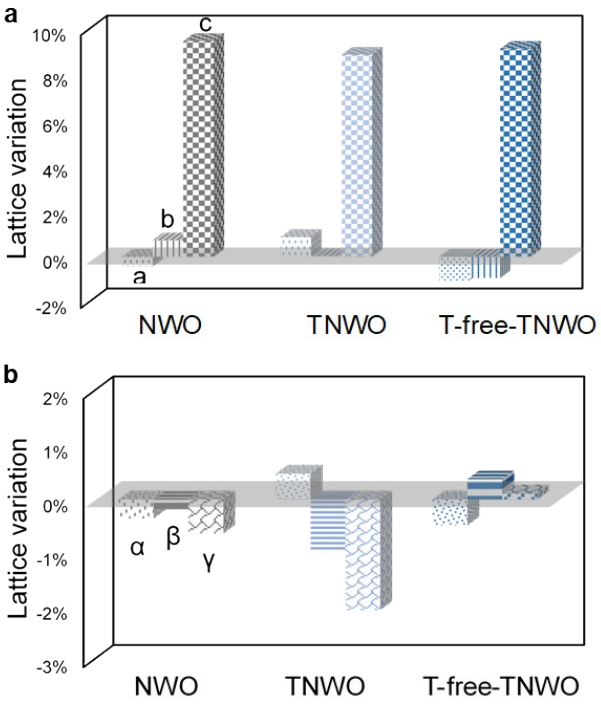

Figure S10. Detailed lattice variation of full Li^+ adsorbed on P and W sites of NWO (blue pattern bars), TNWO (red pattern bars) and T-free-TNWO (green pattern bars). Structurally, all the three models have the largest expansion along *c* axis, but both NWO and TNWO models with WO_4 tetrahedra show similar and larger volume expansions than the T-free-TNWO model, indicating that the tetrahedra with relatively looser structure than other octahedra enlarge the expansion upon Li^+ adsorption.

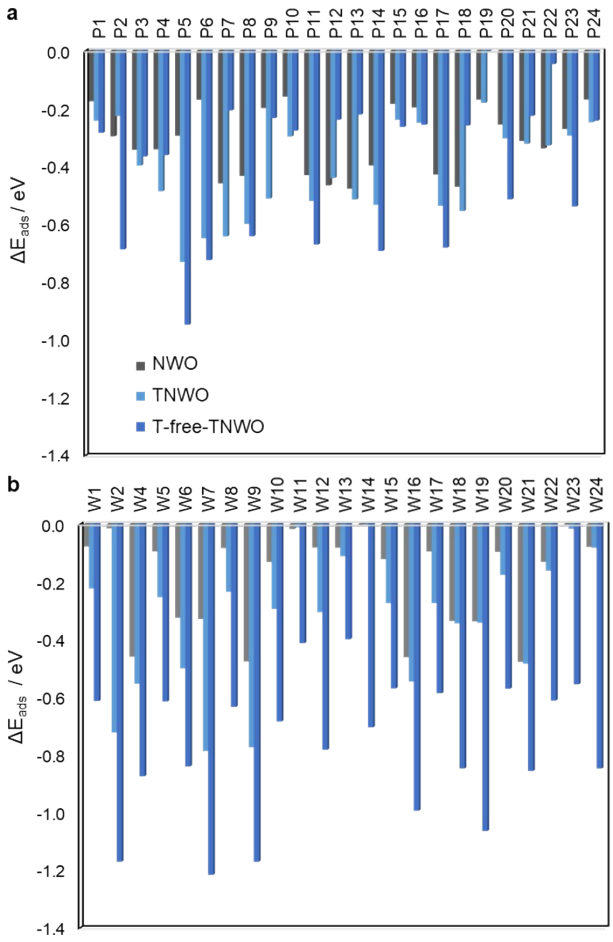

Figure S11. Li^+ adsorption energy variations (ΔE_{ads}) on each (a) P and (b) W sites of NWO (grey bars), TNWO (light blue bars) and T-free-TNWO (dark blue bars). Both the TNWO and T-free-TNWO models have much stronger ΔE_{ads} distributions, while the NWO model has a rather uniform and lower ΔE_{ads}.

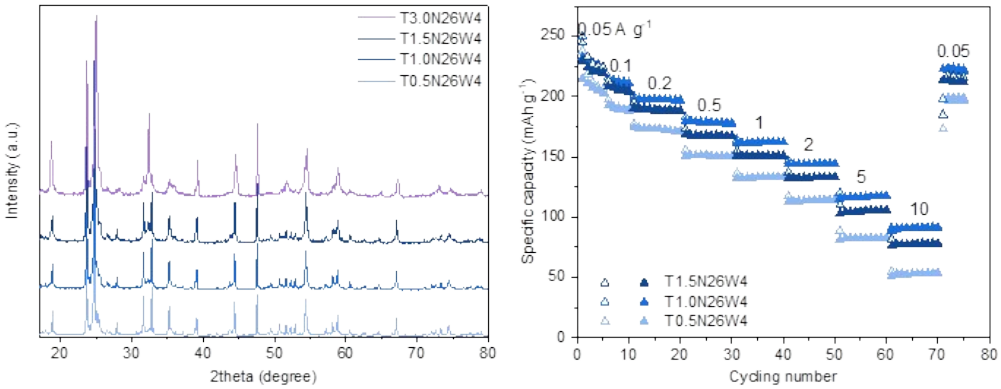

Figure S12. (a) Powder XRD patterns and (b) rate-capabilities for Li^+ storage of the TNWO materials with different cations stiochiometry. XRD patterns show that the TNWO phase can be maintained when the Ti ratio was changed from 0.5 to 1.5. However, the best rate-capability can be only obtained when the TNWO material has the atomic stoichiometric ratio of 1.0:26:4 in our case.

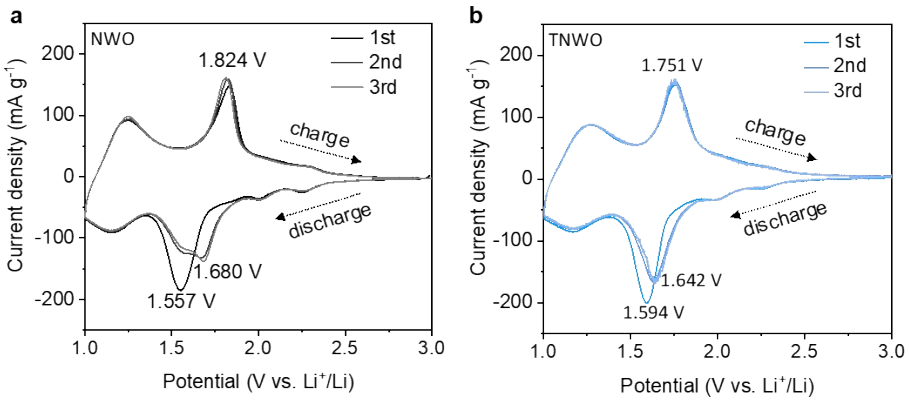

Figure S13. CV curves of the NWO and TNWO bulk anodes at a scan rate of 0.01 mV s^{-1}.

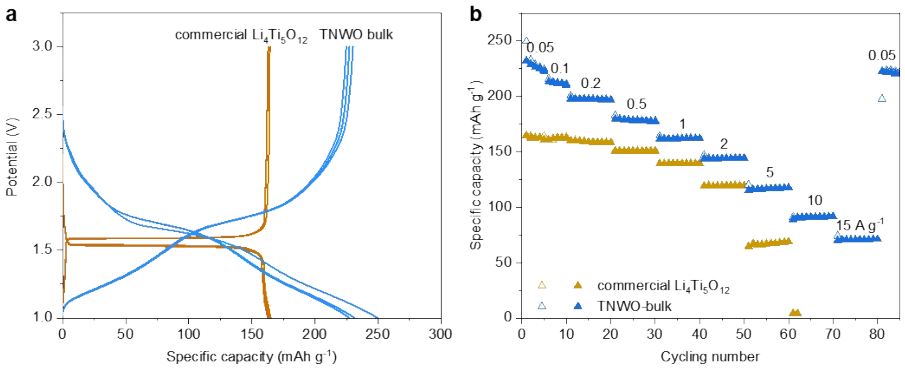

Figure S14. (a) GCD curve at 0.05 A g^{-1} and (b) rate performance comparisons between the commercial $Li_4Ti_5O_{12}$ anode and TNWO bulk anode. Clearly, the TNWO bulk anode shows a comparable average working voltage with the $Li_4Ti_5O_{12}$ anode. However, the TNWO anode delivered a much higher capacities and rate-capability than the $Li_4Ti_5O_{12}$ anode. Especially, the $Li_4Ti_5O_{12}$ anode can't deliver any capacity for Li^+ storage when the current density is over 10 A g^{-1}.

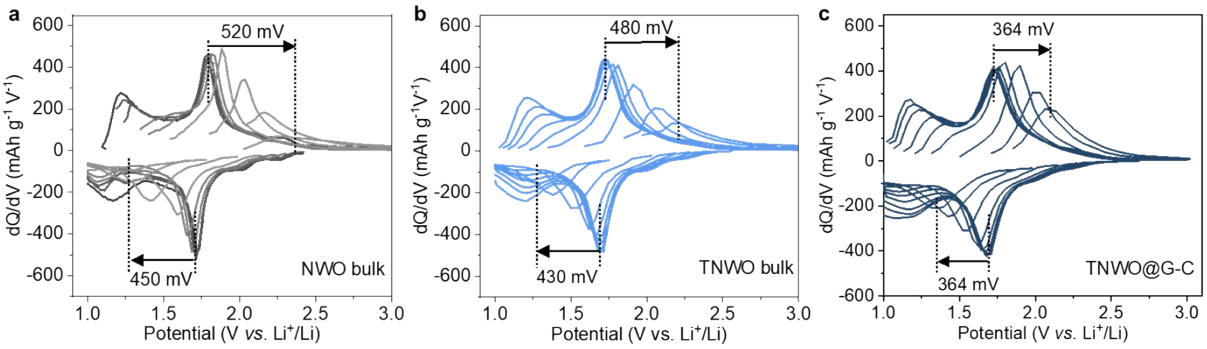

Figure S15. Derived dQ/dV plots from initial GCD curves of the NWO bulk, TNWO bulk and TNWO@G-C composite anodes at each current density increased from 0.05 to 15 A g^{-1}.

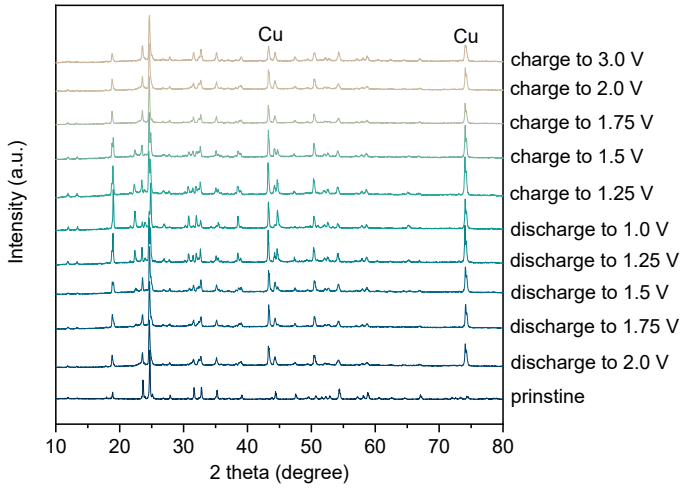

Figure S16. Ex-situ powder XRD patterns at given voltages of the NWO bulk anode during a complete lithation/delithation cycle. Clearly, we can find that the anode underwent a remarkable phase transition started at ~ 1.75 V during discharge process and finished at after 1.75 V during the charge process. This is very different from previous reports about the $Nb_{14}W_3O_{44}$ materials.

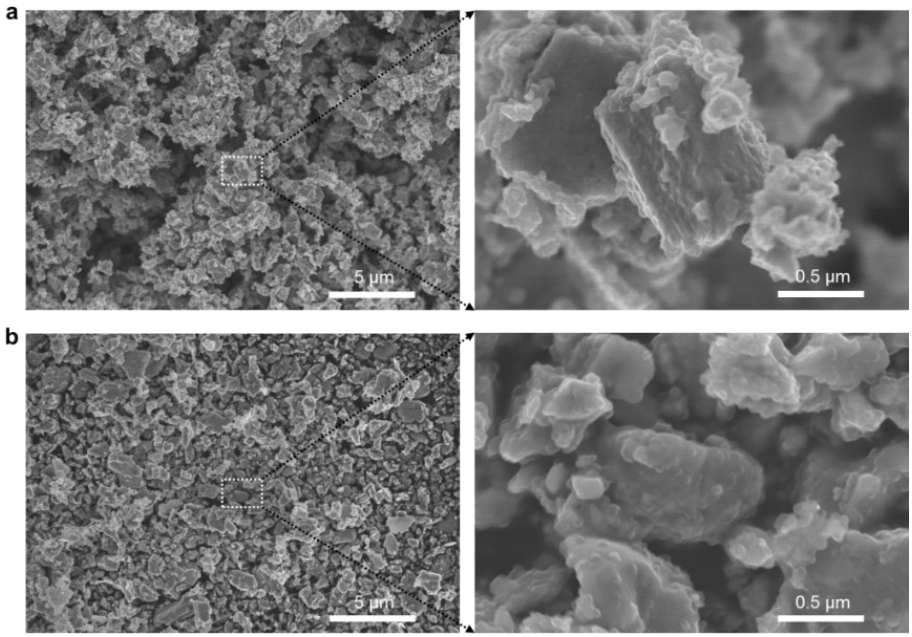

Figure S17. SEM images of (a) TNWO@G-C composite through ball-milling with graphene and (b) TNWO@C composite without graphene additives followed by carbon coating. According to the comparison, clearly, the graphene additive can ensure the dimensional homogeneity of the TNWO particles during the ball-milling.

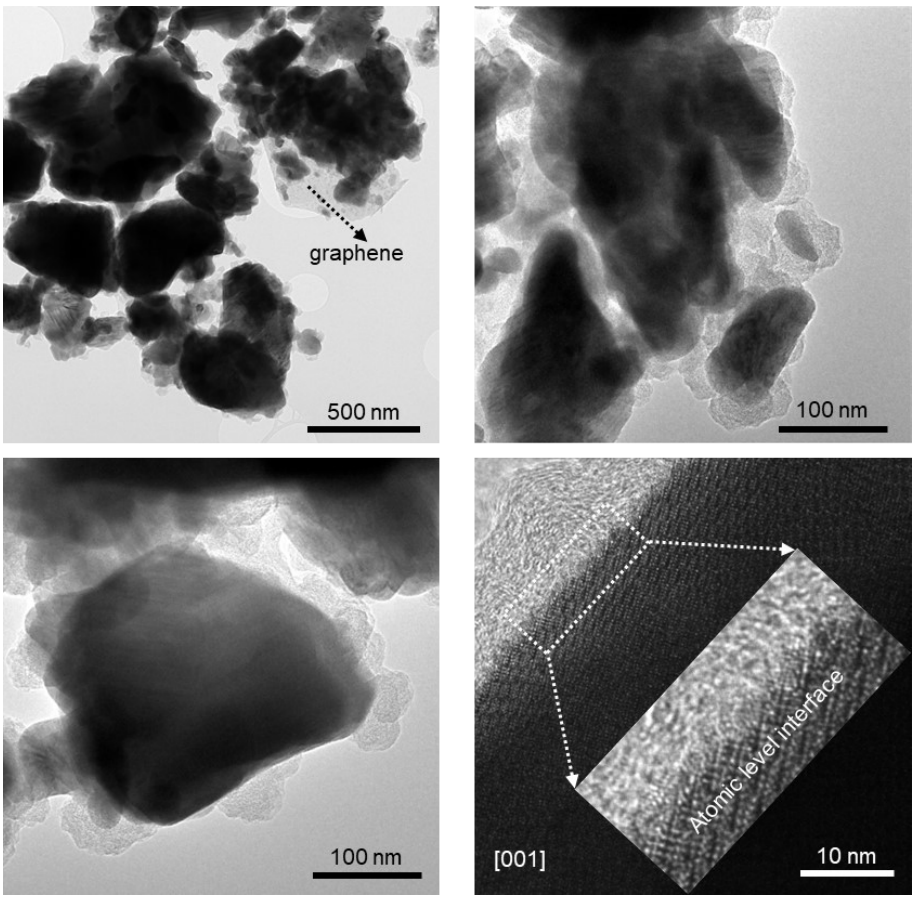

Figure S18. TEM images of the different particles in the TNWO@G-C composite powders. The TNWO nanoparticles in the composite are incompletely covered by a thin amorphous carbon layer, which is 5~10 nm in thickness. Moreover, the carbon layer is adequately infiltrated into the TNWO grain boundaries and formed an atomic-level conductive interface.

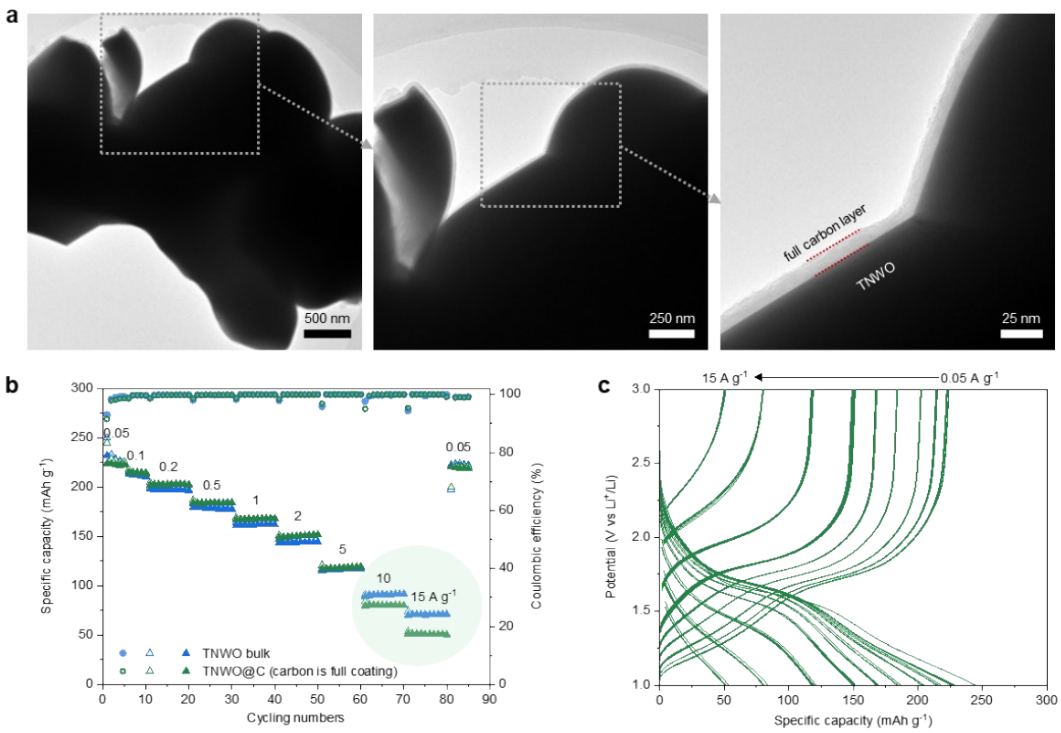

Figure S19. (a) Sequentially enlarged TEM images of the TNWO@C composite powders as a control sample, in which the ball-milled TNWO particle is fully coated by a uniform carbon layer with ~ 10 nm in thickness. (b) Rate-comparison between the TNWO@C composite anode and the pristine TNWO bulk anode. (c) GCD curves of the TNWO@C composite anode at different current densities. Remarkably, compared with the pristine TNWO bulk anode, the Li^+ storage capacities of the TNWO@C composite anode were not increased significantly at low current densities. Moreover, the TNWO@C composite anode delivered lower capacities at 10 and 15 A g^{-1}. We know that the TNWO particle in the composite has much smaller size than the TNWO bulk anode and higher electronic conductivity due to the full carbon coating. Thus, it is reasonable to deduce that the full carbon coating may inhibit the Li^+ diffusion into the bulk phase from the electrolyte especially at high current densities.

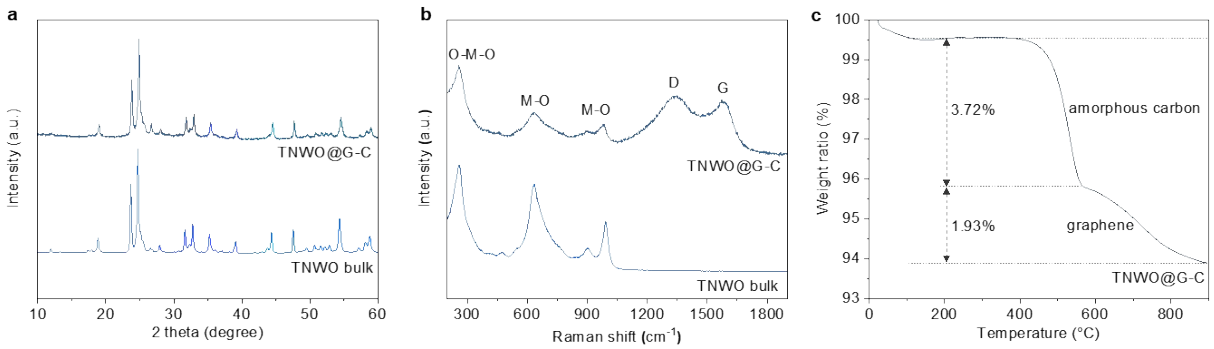

Figure S20. (a) Powder XRD patterns and (b) Raman spectra comparisons between TNWO@G-C composite powders and TNWO bulk powders. (c) TGA curve of the TNWO@G-C composite powders. Clearly, the TNWO component in the composite is maintained well in both of phase structure and chemical composition from the original TNWO bulk powder even though experienced a series of ball-milling and carbon coating. The total mass ratio of the graphene and carbon coating in the composite is measured to be only ~5.65 wt%.

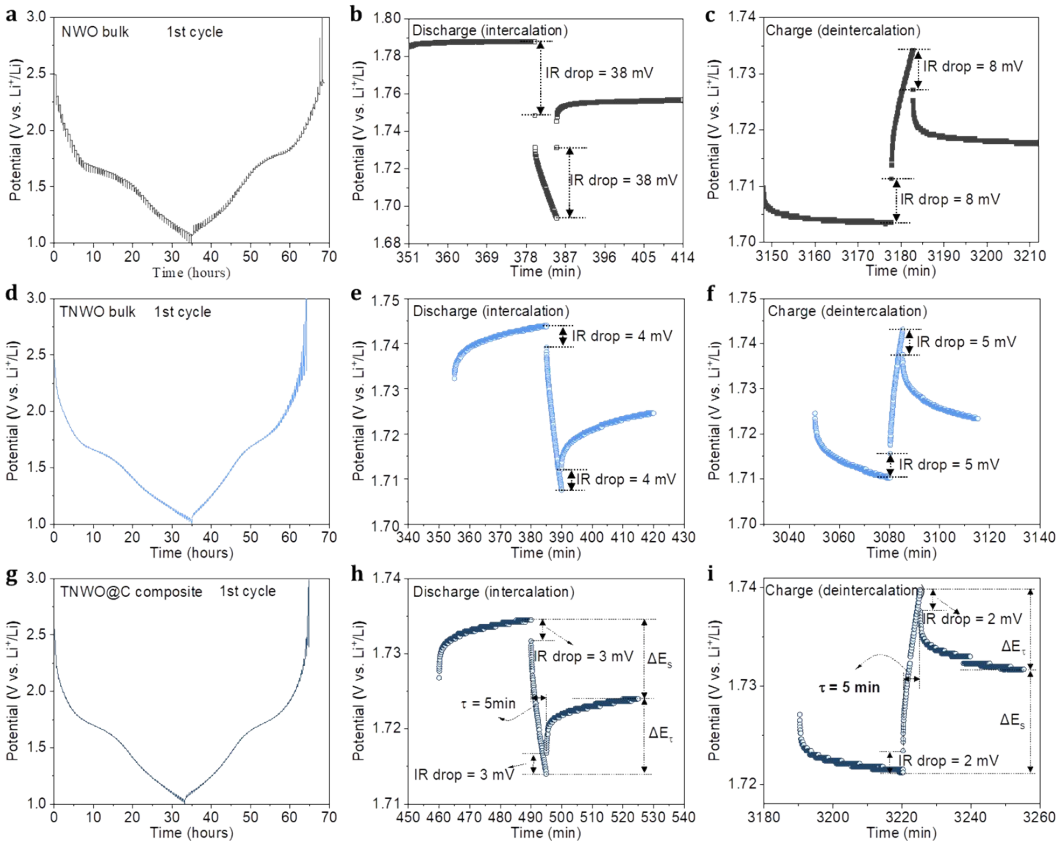

Figure S21. GITT curves and corresponding single-steps during the first discharge (intercalation) - charge (deintercalation) processes of the (a-c) NWO bulk anode, (d-f) TNWO bulk anode and (d-f) TNWO@G-C composite anode. Remarkably, the TNWO@G-C composite anode showed the smallest iR drop values at the beginning of each current pulse among the three anodes.

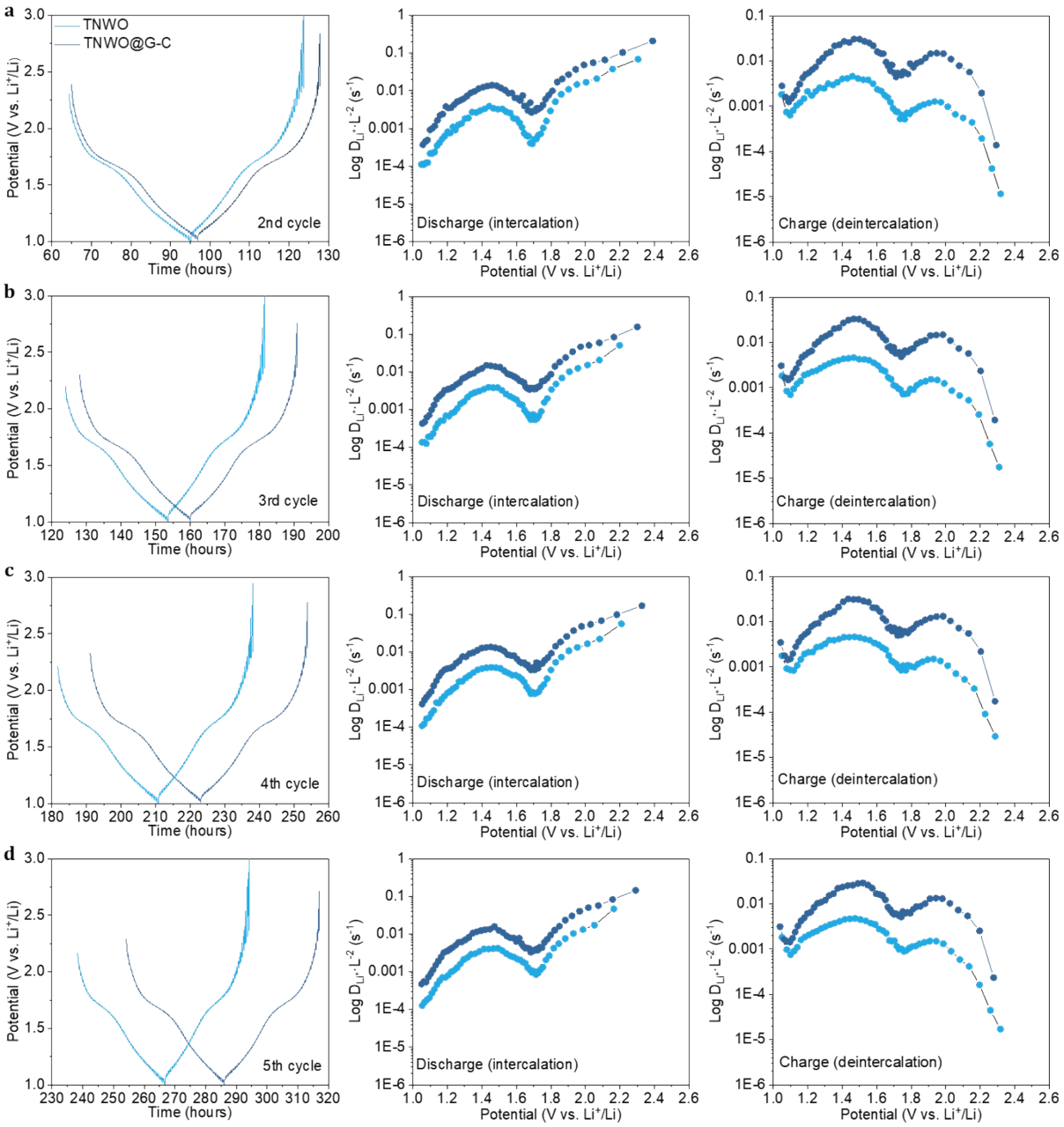

Figure S22. Comparisons of GITT curves and extracted relative Li^+ diffusivities between the TNWO bulk anode and TNWO@G-C composite anode from the 2nd to the 5th discharge-charge cycles. (a) 2nd, (b) 3rd, (c) 4th and (d) 5th cycle. The enhanced Li^+ diffusivity of the TNWO@G-C composite has a robust endurance and can be maintained in the whole test process.

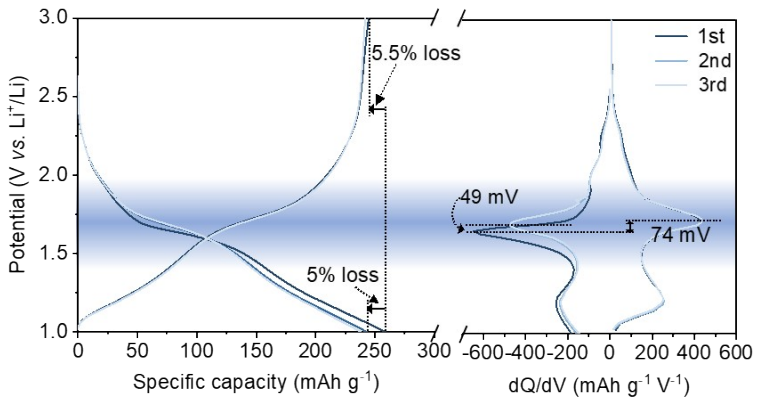

Figure S23. GCD curves and corresponding dQ/dV plots at 0.05 A g^{-1} for the initial three cycles of the TNWO@G-C composite anode.

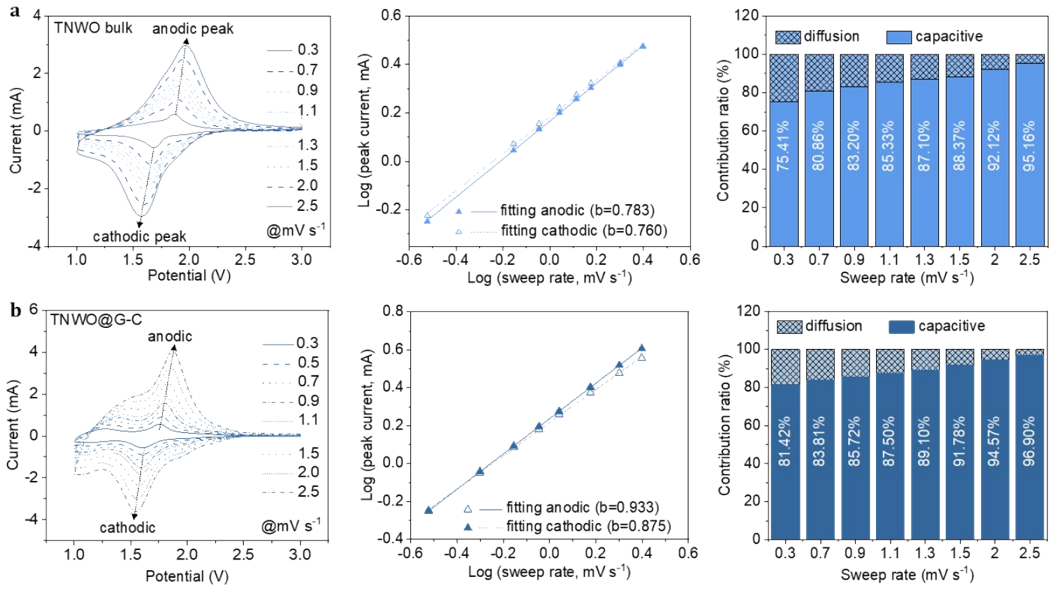

Figure S24. CV curves, normalized cathodic and anodic peak currents and contribution ratios capacities of (a) TNWO bulk and (b) TNWO@G-C composite anodes at increased scan rate from 0.3 and 2.5 mV s^{-1}. It indicates that both anodes showed a remarkable pseudo-capacitive Li^+ intercalation behavior. However, the capacitive contributions to the total capacities of the TNWO@G-C composite anode are significantly higher than the TNWO bulk anode.

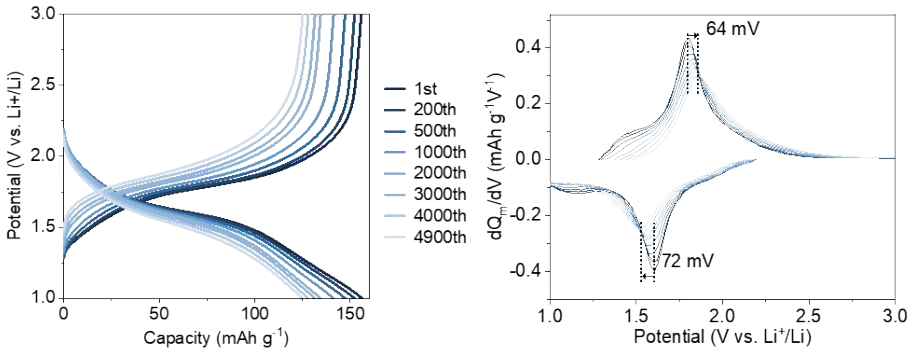

Figure S25. GCD curves and corresponding dQ/dV plots at 5 A g^{-1} for the given cycles during long-term cycling tests of the TNWO@G-C composite anode. Clearly, the composite maintained its Li^+ (de)intercalation behavior very well. The major cathodic and anodic potentials shifted only for 72 and 64 mV, respectively, during the whole 4900 cycles.

References

1 Toby, B. EXPGUI, a graphical user interface for GSAS. *Journal of Applied Crystallography* **34**, 210-213, doi:doi:10.1107/S0021889801002242 (2001).

2 Augustyn, V. *et al.* High-rate electrochemical energy storage through Li+ intercalation pseudocapacitance. *Nat Mater* **12**, 518-522, doi:10.1038/nmat3601 (2013).

3 Yuan, T. *et al.* A hierarchical Ti2Nb10O29 composite electrode for high-power lithium-ion batteries and capacitors. *Mater. Today* **45**, 8-19, doi:10.1016/j.mattod.2020.11.018 (2021).

4 Park, H., Wu, H. B., Song, T., David Lou, X. W. & Paik, U. Porosity-Controlled TiNb2O7Microspheres with Partial Nitridation as A Practical Negative Electrode for High-Power Lithium-Ion Batteries. *Adv. Energy Mater.* **5**, doi:10.1002/aenm.201401945 (2015).

5 Griffith, K. J., Wiaderek, K. M., Cibin, G., Marbella, L. E. & Grey, C. P. Niobium tungsten oxides for high-rate lithium-ion energy storage. *Nature* **559**, 556-563, doi:10.1038/s41586-018-0347-0 (2018).

6 Chen, H. *et al.* Sidorenkite (Na3MnPO4CO3): A New Intercalation Cathode Material for Na-Ion Batteries. *Chem. Mater.* **25**, 2777-2786, doi:10.1021/cm400805q (2013).

7 Yang, X. *et al.* Boosting the Ultrastable High-Na-Content P2-type Layered Cathode Materials with Zero-Strain Cation Storage via a Lithium Dual-Site Substitution Approach. *ACS Nano* **17**, 18616-18628, doi:10.1021/acsnano.3c07625 (2023).

8 Li, H. *et al.* New Insights into Lithium Hopping and Ordering in LiNiO2 Cathodes during Li (De)intercalation. *Chem. Mater.* **33**, 9546-9559, doi:10.1021/acs.chemmater.1c02680 (2021).

9 Kresse, G. & Furthmüller, J. Efficient iterative schemes for ab initio total-energy calculations using a plane-wave basis set. *Physical Review B* **54**, 11169-11186, doi:10.1103/PhysRevB.54.11169 (1996).

10 Kresse, G. & Hafner, J. Ab initio molecular dynamics for liquid metals. *Physical Review B* **47**, 558-561, doi:10.1103/PhysRevB.47.558 (1993).

11 Kresse, G. & Hafner, J. Ab initio molecular-dynamics simulation of the liquid-metal--amorphous-semiconductor transition in germanium. *Physical Review B* **49**, 14251-14269, doi:10.1103/PhysRevB.49.14251 (1994).

12 Ceperley, D. M. & Alder, B. J. Ground State of the Electron Gas by a Stochastic Method. *Physical Review Letters* **45**, 566-569, doi:10.1103/PhysRevLett.45.566 (1980).

13 Perdew, J. P. & Wang, Y. Accurate and simple analytic representation of the electron-gas correlation energy. *Physical Review B* **45**, 13244-13249, doi:10.1103/PhysRevB.45.13244 (1992).

14 Blöchl, P. E. Projector augmented-wave method. *Physical Review B* **50**, 17953-17979, doi:10.1103/PhysRevB.50.17953 (1994).

15 Kresse, G. & Joubert, D. From ultrasoft pseudopotentials to the projector augmented-wave method. *Physical Review B* **59**, 1758-1775, doi:10.1103/PhysRevB.59.1758 (1999).

16 Monkhorst, H. J. & Pack, J. D. Special points for Brillouin-zone integrations. *Physical Review B* **13**, 5188-5192, doi:10.1103/PhysRevB.13.5188 (1976).

17 Kocer, C. P., Griffith, K. J., Grey, C. P. & Morris, A. J. Cation Disorder and Lithium Insertion Mechanism of Wadsley-Roth Crystallographic Shear Phases from First Principles. *J. Am. Chem. Soc.* **141**, 15121-15134, doi:10.1021/jacs.9b06316 (2019).

18 Cheetham, A. K. & Allen, N. C. Cation distribution in the complex oxide, W3Nb14O44; a time-of-flight neutron diffraction study. *Journal of the Chemical Society, Chemical Communications*, 1370-1372, doi:10.1039/C39830001370 (1983).

19 Griffith, K. J. & Grey, C. P. Superionic Lithium Intercalation through 2 × 2 nm2 Columns in the Crystallographic

Shear Phase Nb18W8O69. *Chem. Mater.* **32**, 3860-3868, doi:10.1021/acs.chemmater.9b05403 (2020).

20 Yu, H. *et al.* TiNb2O7 hollow nanofiber anode with superior electrochemical performance in rechargeable lithium ion batteries. *Nano Energy* **38**, 109-117, doi:10.1016/j.nanoen.2017.05.057 (2017).

21 Li, T. *et al.* Operando Raman and DFT Analysis of (De)lithiation in Fast-Charging, Shear-Phase H-Nb2O5. *ACS Energy Lett.* **8**, 3131-3140, doi:10.1021/acsenergylett.3c01031 (2023).

22 Waldron, J. E. L., Green, M. A. & Neumann, D. A. Charge and Spin Ordering in Monoclinic Nb12O29. *Journal of the American Chemical Society* **123**, 5833-5834, doi:10.1021/ja015506b (2001).

23 Zheng, R. *et al.* FeNb11O29 nanotubes: Superior electrochemical energy storage performance and operating mechanism. *Nano Energy* **58**, 399-409, doi:10.1016/j.nanoen.2019.01.065 (2019).

24 Fu, Q. *et al.* Highly conductive CrNb11O29 nanorods for use in high-energy, safe, fast-charging and stable lithium-ion batteries. *Journal of Power Sources* **397**, 231-239, doi:10.1016/j.jpowsour.2018.07.020 (2018).

25 Lin, C. *et al.* Intercalating Ti2Nb14O39 Anode Materials for Fast-Charging, High-Capacity and Safe Lithium-Ion Batteries. *Small* **13**, doi:10.1002/smll.201702903 (2017).

26 Yu, H. *et al.* Deep insights into kinetics and structural evolution of nitrogen-doped carbon coated TiNb24O62 nanowires as high-performance lithium container. *Nano Energy* **54**, 227-237, doi:10.1016/j.nanoen.2018.10.025 (2018).

27 Yan, L. *et al.* Electrospun WNb12O33 nanowires: superior lithium storage capability and their working mechanism. *Journal of Materials Chemistry A* **5**, 8972-8980, doi:10.1039/c7ta01784g (2017).

28 Yang, Y. *et al.* Achieving Ultrahigh-Rate and High-Safety Li(+) Storage Based on Interconnected Tunnel Structure in Micro-Size Niobium Tungsten Oxides. *Adv. Mater.* **32**, e1905295, doi:10.1002/adma.201905295 (2020).

29 Fu, Q. *et al.* A low-strain V3Nb17O50 anode compound for superior Li+ storage. *Energy Storage Materials* **30**, 401-411, doi:10.1016/j.ensm.2020.05.012 (2020).